



Contents lists available at ScienceDirect

Chemical Engineering Research and Design

IChemE

journal homepage: [www.elsevier.com/locate/cherd](http://www.elsevier.com/locate/cherd)

# Effect of nozzle external geometry on the pressure and shear stress exerted on the surface being gauged in fluid dynamic gauging

J.M. Peralta<sup>a,b</sup>, Y.M.J. Chew<sup>c,\*</sup>, D.I. Wilson<sup>b</sup>

<sup>a</sup> Instituto de Desarrollo Tecnológico para la Industria Química (INTEC), Universidad Nacional del Litoral – CONICET, Güemes 3450, S3000GLN, Santa Fe, Argentina

<sup>b</sup> Department of Chemical Engineering and Biotechnology, University of Cambridge, New Museums Site, Pembroke Street, Cambridge CB2 3RA, UK

<sup>c</sup> Department of Chemical Engineering, University of Bath, Building 9 West, Claverton Down, Bath BA2 7AY, UK

## ABSTRACT

Fluid dynamic gauging (FDG) is an experimental technique that exploits the behaviour of a suction flow through a nozzle located near a fouling deposit to determine the thickness of the layer. The nozzle does not contact the layer but the shear stress imposed by the flow could cause it to deform. The effect of the external shape of the nozzle on the stresses on the surface being gauged was investigated using computational fluid dynamics (CFD) simulations. Different nozzle shapes were studied using a 2D axi-symmetric computational domain. CFD results were validated by comparison with (i) a set of experimental values for the normal stresses acting on the gauged surface, and (ii) an analytical solution for the limiting case approached under certain conditions. The results obtained for different simple geometries show that certain desirable pressure and surface shear stress distributions can be obtained by selection of the appropriate external nozzle shape.

© 2011 The Institution of Chemical Engineers. Published by Elsevier B.V. All rights reserved.

**Keywords:** CFD; Fluid dynamic gauging; Sensor; Shear stress

## 1. Introduction

Fouling is generally defined as the unwanted deposition of species from process fluids on to equipment surfaces (Epstein, 1983). The growth of such deposits can cause large reductions in the thermal and hydraulic performance of process units. In the food and biotechnology sectors, fouling deposits are often soft and fragile as their microstructure consists of high liquid fraction gels or biofilms. These deposits are highly deformable and their thickness is difficult to measure if they are removed from their native environment. Thus, a technique for measuring thickness that can be used on immersed layers *in situ* without altering the deposit is needed.

Fluid dynamic gauging (FDG), developed by Tuladhar *et al.* (2000), is a relatively novel technique that can be used to estimate the thickness of a soft deposit layer immersed in liquid *in situ* and in real time without contacting the layer. The sys-

tem consists of a nozzle that withdraws liquid from the region near the deposit surface (Fig. 1). For a certain range of distances between the nozzle and the surface (labeled the clearance,  $h$ ), the mass flow rate ( $\dot{m}$ ) through the nozzle is usefully sensitive to  $h$  (Fig. 1(b)). The thickness of the deposit,  $\delta$ , can be calculated from the difference between the position of the nozzle relative to the substrate,  $h_0$ , and the clearance between the nozzle and the deposit layer,  $h$ , inferred from the flow rate. This technique provides high accuracy thickness measurement (ca.  $\pm 5 \mu\text{m}$ , Gordon *et al.*, 2010).

FDG has been applied to a number of different cases of fouling and cleaning since 2000 (see, for example, Hooper *et al.*, 2006; Saikhwan *et al.*, 2007; Sahoo *et al.*, 2008). The flow of liquid into the nozzle exerts a shear stress on the bounding surfaces, i.e. the nozzle wall and the deposit. The flows lie in the viscous regime, so these stresses can be estimated with high confidence by computational fluid dynamics

\* Corresponding author. Tel.: +44 01225 386132; fax: +44 01225 385713.

E-mail address: [jc604@bath.ac.uk](mailto:jc604@bath.ac.uk) (Y.M.J. Chew).

Received 8 March 2011; Received in revised form 23 May 2011; Accepted 22 June 2011

### Nomenclature

$d_t$	nozzle throat diameter (m)
$\underline{F}$	volume force field ( $\text{N m}^{-3}$ )
$H$	hydrostatic head (m)
$h$	clearance between the nozzle and the deposit layer (m)
$h_0$	clearance between the nozzle and the surface (m)
$\dot{m}$	mass flow rate ( $\text{kg s}^{-1}$ )
$p$	pressure at the gauged surface (Pa)
$p_a$	pressure at the inlet of the nozzle (Pa)
$p_{ave}$	area-averaged pressure at the gauged surface (Pa)
$p_b$	pressure at the exit of the tube (Pa)
$p_o$	pressure at the stagnation point on the gauged surface (Pa)
$p^*$	dimensionless pressure at the gauged surface ( $p/p_o$ )
$r$	radial position on the gauged surface (m)
$R$	radius of the tube (m)
$R^*$	dimensionless radial position on the gauged surface ( $r/R$ )
$Re$	Reynolds number ( $2\dot{m}/\pi\mu R$ )
$r_i$	inner radius of the nozzle (m)
$r_o$	outer radius of the nozzle (m)
$t$	time (s)
$\underline{u}$	velocity vector ( $\text{m s}^{-1}$ )
$u_z$	velocity component in z-direction ( $\text{m s}^{-1}$ )
$u_{z,ave}$	area-averaged velocity component in z-direction ( $\text{m s}^{-1}$ )
$w$	length of the nozzle rim (m)
$z$	axial position (m)
<b>Greek symbols</b>	
$\alpha$	angle of the internal divergent zone of the nozzle ( $^\circ$ )
$\delta$	thickness of the deposit (m)
$\theta$	angle of the external surface of the nozzle ( $^\circ$ )
$\lambda$	length of nozzle exit (m)
$\mu$	dynamic viscosity (Pa s)
$\rho$	density ( $\text{kg m}^{-3}$ )
$\underline{\tau}$	shear stress tensor (Pa)
$\tau$	shear stress on the gauged surface (Pa)
$\tau_{ave}$	area-averaged shear stress on the gauged surface (Pa)
$\tau_{max}$	maximum value of $\tau_{rz}$ on the gauged surface (Pa)
$\tau_{theor}$	theoretical shear stress defined by Eq. (5) (Pa)
$\tau^*$	dimensionless shear stress on the gauged surface ( $\tau_{rz}/\tau_{max}$ )

(CFD) simulations. Comparing the deposit thickness before and after gauging – at known stress conditions – provides a method for assessing the strength of the deposit. Chew et al. (2004a,b) used this approach to track the effect of ageing on the strength of tomato paste foulant layers: they commented that the external shape of the nozzle – a simple truncated cone in Fig. 1 – could be manipulated to give different stress distributions. Ideally, one shape may give high sensitivity for thickness measurement and another an even stress distribution desired for strength testing. The objective of this work was to study,

using CFD simulation, the effect of the shape of the external part of the FDG nozzle on the shear stress and pressure profiles imposed on the gauged surface, with the long term aim of identifying optimal designs for thickness and/or strength measurement.

## 2. Experimental

The reliability of the simulations was tested by comparing results with experimental measurements of the pressure exerted on the gauged surface, obtained using the apparatus described by Chew et al. (2004b). This featured a nozzle of conical external shape, labeled type N2 in this work, with dimensions (see Fig. 1)  $R=10$  mm,  $d_t=5$  mm,  $w=5$  mm,  $\alpha=45^\circ$ ,  $\lambda=0.5$  mm and  $\theta=60^\circ$ . The apparatus (Fig. 2) consisted of a nozzle located in a rectangular tank of dimensions (width  $\times$  depth  $\times$  height) 300 mm  $\times$  300 mm  $\times$  250 mm and connected to a siphon tube. Both the tank and the nozzle were constructed from Perspex.

The test liquid was water at  $20 \pm 2^\circ\text{C}$ , maintained at a constant level in the tank by a weir. The position of the nozzle was controlled in the horizontal direction by a traversing screw connected to a Vernier scale ( $\pm 50 \mu\text{m}$ ; Mitutoyo, Japan) and in the vertical direction by a micrometer ( $\pm 5 \mu\text{m}$ ; Mitutoyo, Japan). The flow rate through the nozzle was set by the hydrostatic head,  $H$ , imposed by the difference in liquid levels between the tank and the end of the siphon tube. Unless otherwise stated, the experiments were performed at  $H=800$  mm. The flow rate was determined by catch-and-weigh using an electronic balance ( $\pm 0.001$  g). The local pressure on the surface exerted by the gauging flow was measured via a 0.5 mm diameter pressure tapping connected to an inclined U-tube manometer filled with the process liquid. The angle of inclination was  $30^\circ$  from the vertical axis. The pressure was measured at different positions, moving the gauging nozzle across the pressure tapping at fixed clearance,  $h$ , so that the pressure profile was recorded across the range  $-2R < r < +2R$ .

## 3. Numerical simulation

### 3.1. Nozzle geometries

The shapes of the nozzles explored in this work are shown in Fig. 3. These geometries were selected based on their simplicity and their ease of fabrication. All nozzles featured the same internal geometry as this has no effect on the pressure and/or shear stress exerted on the gauged surface (Chew et al., 2004a).

### 3.2. Computational domain and model

Simulations were carried out using a 2D axi-symmetric computational domain based on that employed by Chew et al. (2004a) for modelling quasi-static FDG systems. Quasi-static here refers to the absence of a bulk convective flow apart from that induced by the gauging action. The flow throughout the domain was assumed to be laminar as the Reynolds numbers at the tube exit considered were less than 500. The governing equations were

$$\rho \frac{\partial \underline{u}}{\partial t} - \nabla \cdot \underline{\tau} + \rho(\underline{u} \cdot \nabla)\underline{u} + \nabla p = \underline{F} \quad (\text{Navier–Stokes}) \quad (1)$$

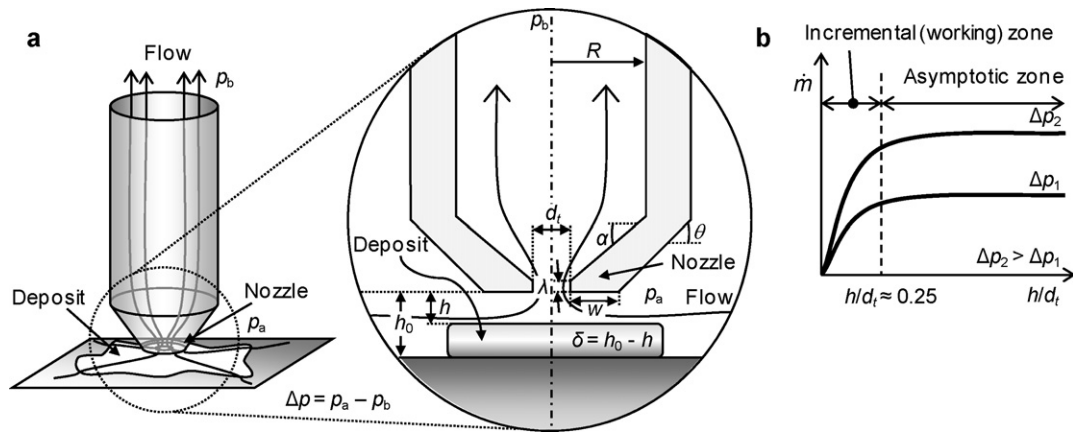


Fig. 1 – Principles of fluid dynamic gauging. (a) Schematic of nozzle, with inset showing key dimensions; (b) calibration curves showing relationship between mass flow rate,  $\dot{m}$ , and dimensionless clearance,  $h/d_t$ .

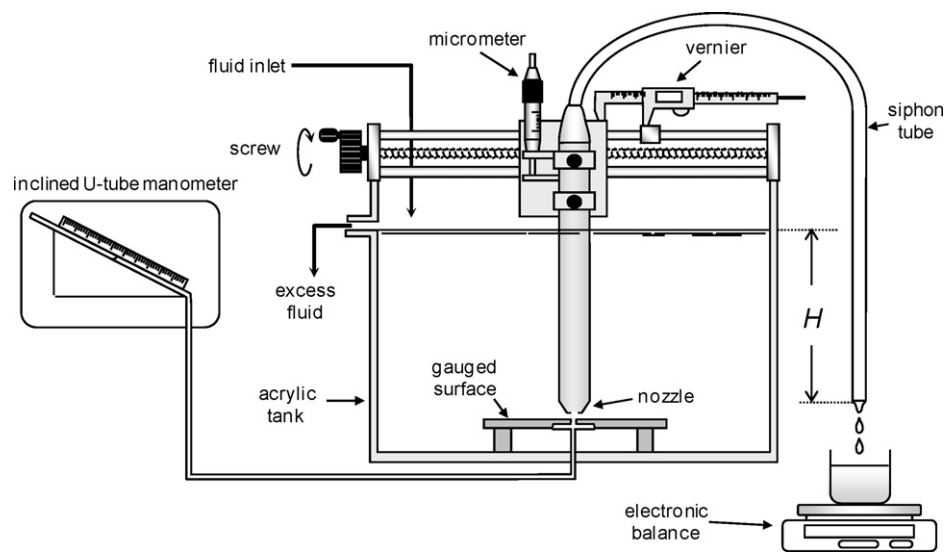


Fig. 2 – Schematic of the gauging apparatus.

and

$$\nabla \cdot \underline{u} = 0 \quad (\text{Continuity}) \quad (2)$$

where  $\rho$  is the density,  $p$  the pressure,  $\underline{u}$  is the velocity vector,  $\underline{\tau}$  is the shear stress tensor, and  $\underline{F}$  is a volume force field (e.g. gravity) set to be zero in the simulations reported here. The liquid is Newtonian, so the shear stress tensor can be estimated from

$$\underline{\tau} = \mu [\nabla \underline{u} + (\nabla \underline{u})^T] \quad (3)$$

where  $(\nabla \underline{u})^T$  is the transpose of  $\nabla \underline{u}$ .

Fig. 4 shows a representative computational domain employing cylindrical co-ordinates. The boundary conditions are defined on Fig. 4(a) and feature non-slip, impermeable walls. Liquid enters the domain through the open boundary AB and leaves through the gauging tube as a fully developed Poiseuille flow. Chew et al. (2004a) investigated the effect of defining the open boundary as AB, ABC and BC, and reported that the former gave good agreement with experimental observations with least computational effort.

Simulations were performed at different values of Reynolds number,  $Re$ , defined as  $2\dot{m}/\pi\mu R$  where  $\mu$  is the dynamic viscosity,  $R$  the radius of the exit tube of the nozzle,  $\rho$  the density and  $\dot{m}$  the mass flow rate.  $Re$  values of 50, 100, 150, 200, 300, 400 and 500 were investigated, in combination with shapes

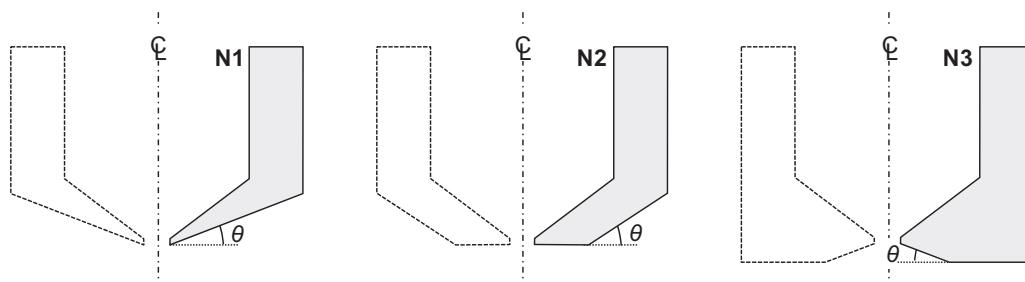
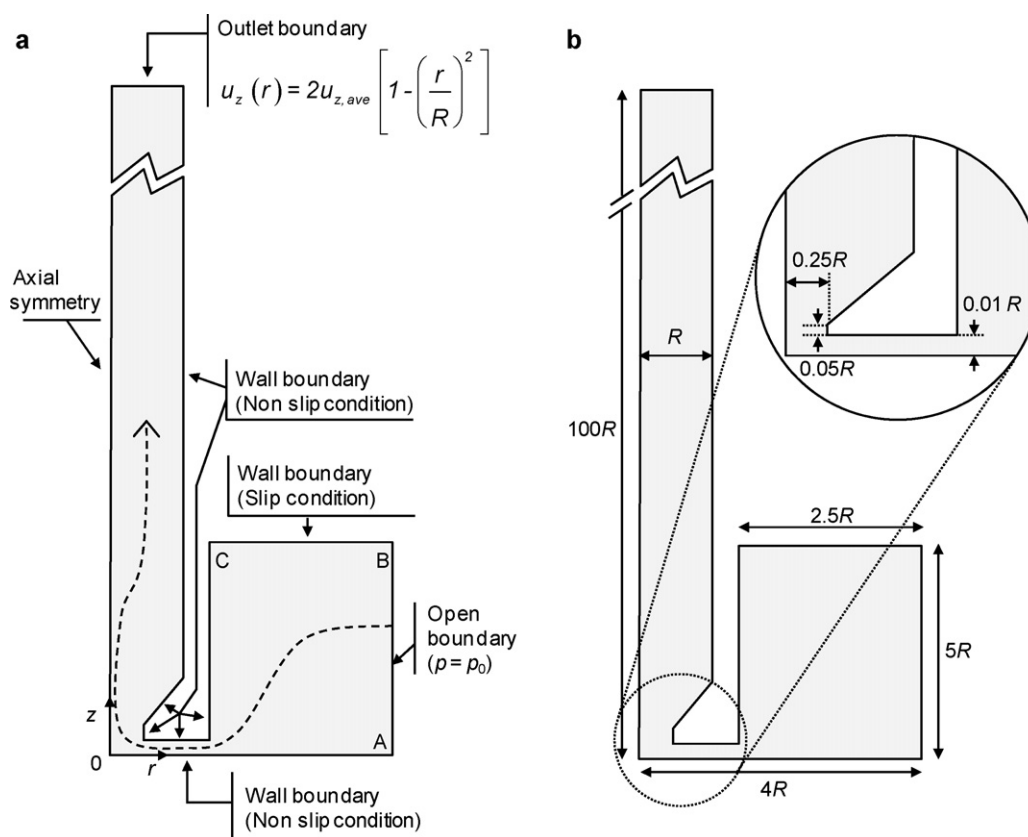


Fig. 3 – Nozzle shapes investigated in this study.



**Fig. 4 – Simulation geometry showing (a) boundary conditions and (b) domain dimensions for nozzle shape N1 with  $\theta = 0^\circ$  used in the CFD simulations. The radius of the exit tube of the nozzle was  $R = 10$  mm. Dashed line represents the fluid path through the nozzle.**

defined by the angle subtended by the non-horizontal surface part of the nozzle facing the gauged surface,  $\theta$  (see Fig. 3). For all simulations the closest approach between the nozzle and the gauged surface was set to  $h/d_t = 0.2$ . This clearance lies within the incremental zone depicted in Fig. 1(b) and is typical of the value used in thickness measurement, imposing a low shear stress on the substrate and thereby minimizing deformation.

The domain was discretised using a triangular mesh. In regions where the velocity gradients were large and varying strongly spatially (e.g. the gap between the nozzle and the gauged surface) a dense mesh was used (Fig. 5). The commercial finite-element-based software COMSOL Multiphysics 3.5a and 4 (COMSOL Ltd., Hatfield, United Kingdom) was used to perform the CFD simulations. Around 100 simulations were carried out on a 2.4 GHz desktop PC equipped with 5 processors and 4 GB of RAM. Each simulation took approximately 5 min to converge. Iterations were stopped when the error between two successive iterations, computed as the weighted Euclidean norm, was less than  $10^{-6}$  (COMSOL, 2008).

## 4. Results and discussion

### 4.1. Model validation

Model validation comprised testing the independency of the studied variables on the mesh density and comparison of simulation results with experimental observations.

#### 4.1.1. Mesh independency

The density of the mesh used to map the entire domain was increased from 340 to 18 000 elements. The variables selected to assess the independency test were the average pressure and

shear stress values exerted on the gauged surface. Fig. 6 shows the results obtained for the area-averaged (a) pressure and (b) shear stress under the nozzle rim for a type N1 nozzle with  $\theta = 0^\circ$ . The area-averaged values were evaluated using

$$\phi_{ave} = \frac{2}{(r_o^2 - r_i^2)} \int_{r_i}^{r_o} \phi r dr \quad (4)$$

where  $r_o$  and  $r_i$  are the outer and inner radius of the nozzle, respectively, and  $\phi$  is the local value of the variable being averaged (e.g.  $\tau$  or  $p$ ).

The figure shows convergence is reached as the mesh density increased, with values reaching a plateau after about 3000 elements for  $\tau_{ave}$  and  $\sim 7000$  for  $p_{ave}$ . The results presented in subsequent plots employed more than 7000 elements to ensure mesh independency. A second measure of simulation convergence is comparison of mass flow rate into and leaving the domain: these agreed within 0.05% for all simulations presented here.

#### 4.1.2. Comparison with experiment

Simulations are presented for comparison with two sets of experimental data collected using a type N2 nozzle with  $\theta = 60^\circ$ . Fig. 7(a) shows the stagnation pressure,  $p_0$ , measured at the surface on the axis ( $r = 0$  in Fig. 4) for a set hydrostatic pressure driving force at different values of clearance,  $h$ . The pressure decreases rapidly as  $h/d_t$  increases until  $h/d_t \sim 0.25$ , above which the decrease is more gradual. The corresponding mass flow rate increases as  $h/d_t$  increases, plateauing off above  $h/d_t \sim 0.25$ . The experimental data show very good agreement with the simulation, indicating that the latter gives a good

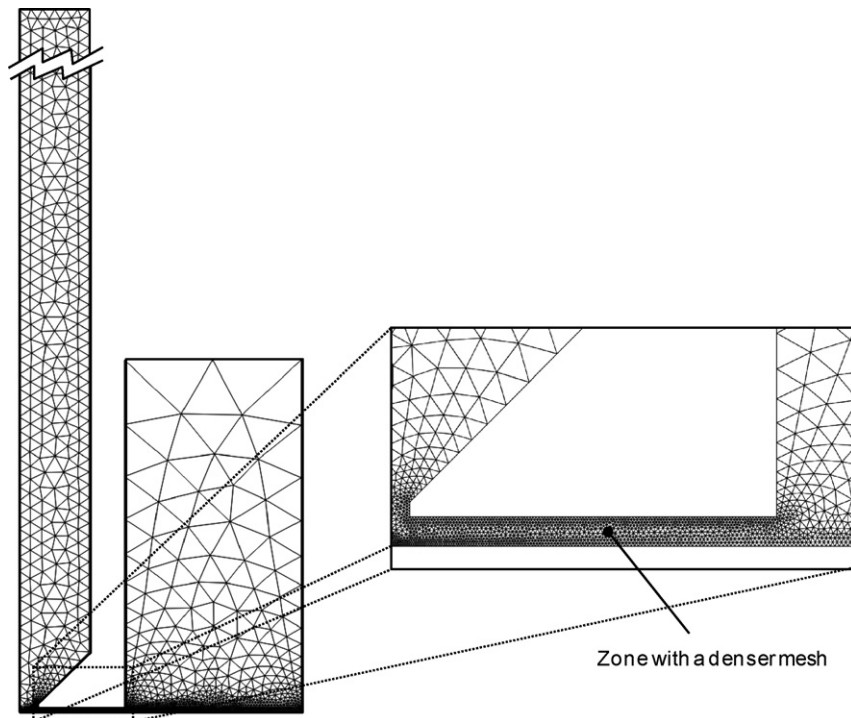


**Fig. 5 – Mesh used for the simulations, for nozzle shape N1 with  $\theta = 0^\circ$ ,  $h/d_t = 0.2$ . A high mesh density is employed under the nozzle rim, in the throat, and along the base.**

description of the *overall* behaviour of the gauging system. The associated mass flow rate and discharge coefficients show equally good agreement (data not reported).

The agreement between the measured pressure distribution and the simulated values in Fig. 7(b) is equally good. Data are presented for two values of  $h/d_t$ , both of which lie within the region of interest for experimental measurements. The comparisons with experimental data are as good or superior to those presented by Chew et al. (2004a), who employed the PDE solver Fastflo™ to solve the governing equations. The use of the code to study nozzle geometry is therefore justified.

#### 4.1.3. Comparison with analytical solution

A final verification of the simulation is to compare its predictions with the analytical result for radial flow between two parallel disks presented by Middleman (1998). Inspection of Fig. 3 shows that the region underneath the nozzle rim approaches this geometry as  $\theta \rightarrow 0$  for all nozzle types. The

analytical solution for the shear stress on the wall in this case is given by

$$\tau_{theor} = \frac{3\mu^2 Re}{2\rho h^2} \frac{1}{r} \quad (5)$$

giving an average shear stress under the nozzle rim as

$$\tau_{ave} = \frac{3\mu^2 Re}{\rho h^2 (r_o + r_i)} \quad (6)$$

where  $Re$  is the Reynolds number, and  $r$  is the radial position on the gauged surface. The shear stress distribution was evaluated for a number of  $Re$  values within the range of validity of equation (5), with  $Re < 500$ . The values of  $Re$  and  $h$  set the flow rate for use in the CFD simulation. Fig. 8 shows excellent agreement between the analytical solution and the simulation, further confirming its applicability for these studies.

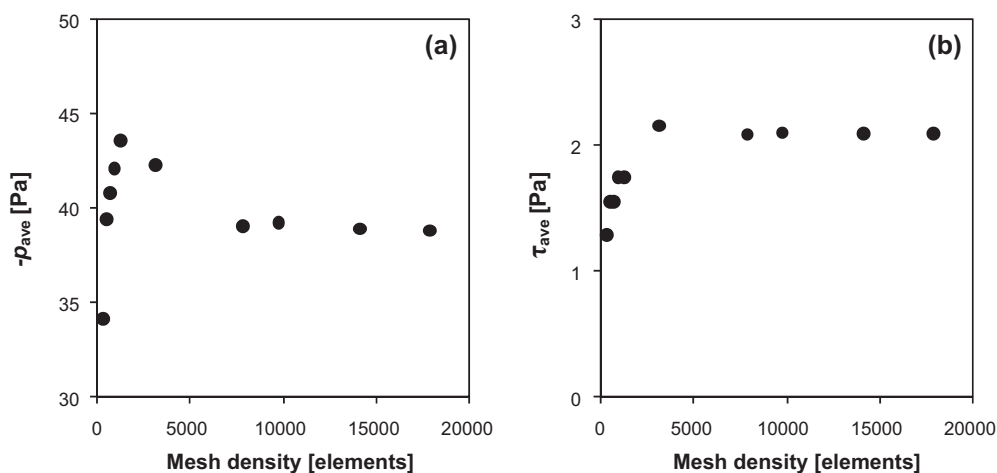


**Fig. 6 – Effect of mesh density on (a) area-averaged pressure and (b) shear stress, calculated using Eq. (4), for nozzle N1 with  $\theta = 0^\circ$ .**



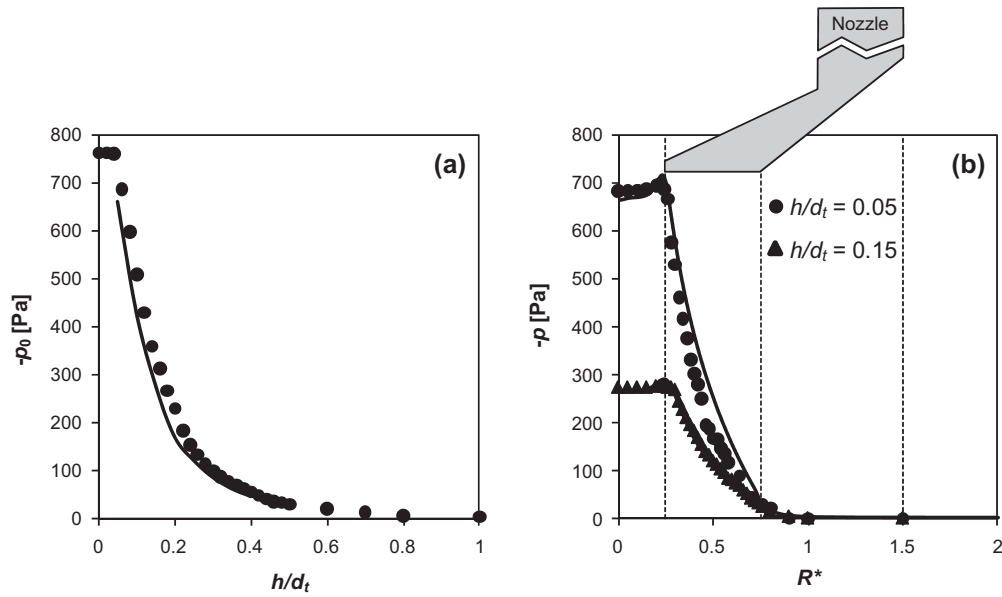


**Fig. 7** – Comparison of experimental pressure data sets with simulation for a type N2 nozzle with  $\theta = 60^\circ$ . (a) Pressure at stagnation point,  $p_0$ , as a function of  $h/d_t$ . (b) Pressure distribution under the nozzle, plotted against dimensionless radial position  $R^*$ , defined as  $R^* = r/R$  at two different  $h/d_t$  values. Symbols correspond to experimental values and loci correspond to simulations. For (a) and (b) the hydrostatic head ( $H$ ) was set to 800 mm. The relative average standard deviation of the experimental pressure data was 5%.

#### 4.2. Effect of nozzle shape

##### 4.2.1. Pressure

Nozzle N1 represents the simplest configuration. When the angle of nozzle inclination relative to the gauged surface,  $\theta$ , is positive, the flow around the external part of the nozzle is convergent in both the vertical and radial directions. When  $\theta$  is negative, i.e. a recessed orifice, the clearance increases as the flow approaches the orifice and the point closest to the surface – which determines the clearance,  $h$ , – is the outer rim of the nozzle. This gives rise to different flow patterns and stress distributions. Fig. 9(a) shows the dimensionless pressure ( $p^* = p/p_0$ ) against radial position for different values of  $\theta$  for two values of  $Re$ . In general, the pressure profiles exhibit a maximum between the stagnation point at  $R^* = 0$  and the inner radius of the nozzle throat, at  $R^* = 0.25$ . This maximum was a peak for positive  $\theta$ , at the position where the fluid turns

abruptly to enter to the nozzle. The peak is not observed with negative  $\theta$  as the flow is not subject to the sharp change in direction at the orifice. Differences between positive and negative  $\theta$  are evident at the outer rim. For positive  $\theta$  there is a monotonic decay with increasing radial position, whereas a secondary peak (that starts as a shoulder for  $\theta = -5^\circ$ ) is evident with negative  $\theta$ . This is particularly evident at higher  $Re$  in Fig. 9(a, ii). The shape of the profiles changes from convex to concave in the range  $-5^\circ < \theta < 0$  as the region of greatest pressure drop shifts from the inner to the outer rim. For all  $Re$  values studied, the pressure profiles were most sensitive to  $\theta$  in the range  $-10^\circ < \theta < 5^\circ$ . The effect of changing  $\theta$  was progressively smaller outside this range, suggesting asymptotic behaviour.

Type N2 nozzles feature a horizontal rim near the nozzle throat and a convergent outer section. The dimensionless pressure distributions in Fig. 9(b) are similar to those obtained

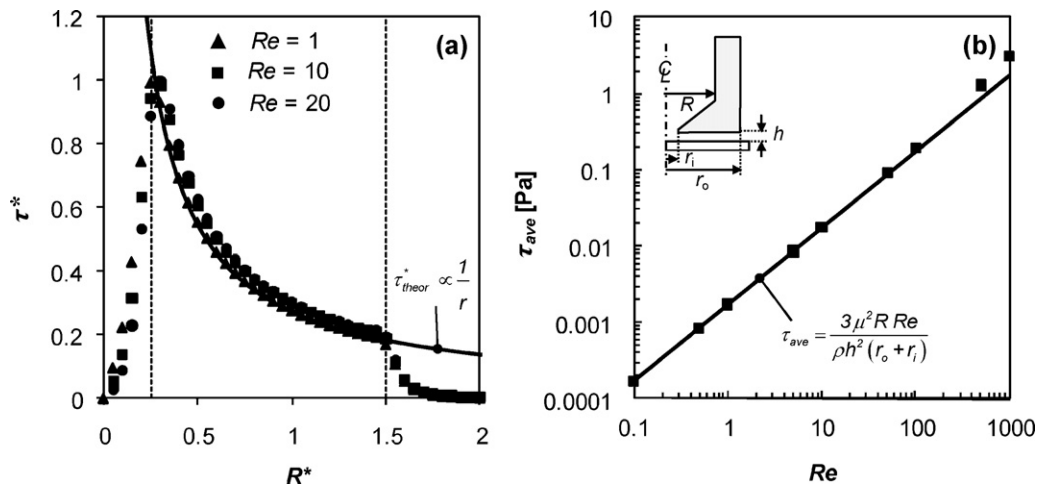


**Fig. 8** – Comparison of analytical approximation with simulation. (a) Dimensionless shear stress ( $\tau^* = \tau_{rz}/\tau_{max}$ ) as a function of  $R^*$  for different  $Re$  ( $h/d_t = 0.2$ ) for nozzle N1 with  $\theta = 0^\circ$ ; and (b) area-averaged shear stress as a function of  $Re$  at  $h/d_t = 0.2$  for nozzle N1 with  $\theta = 0^\circ$ . Symbols represent simulation values and loci show theoretical results (Eqs. (4) and (5)).

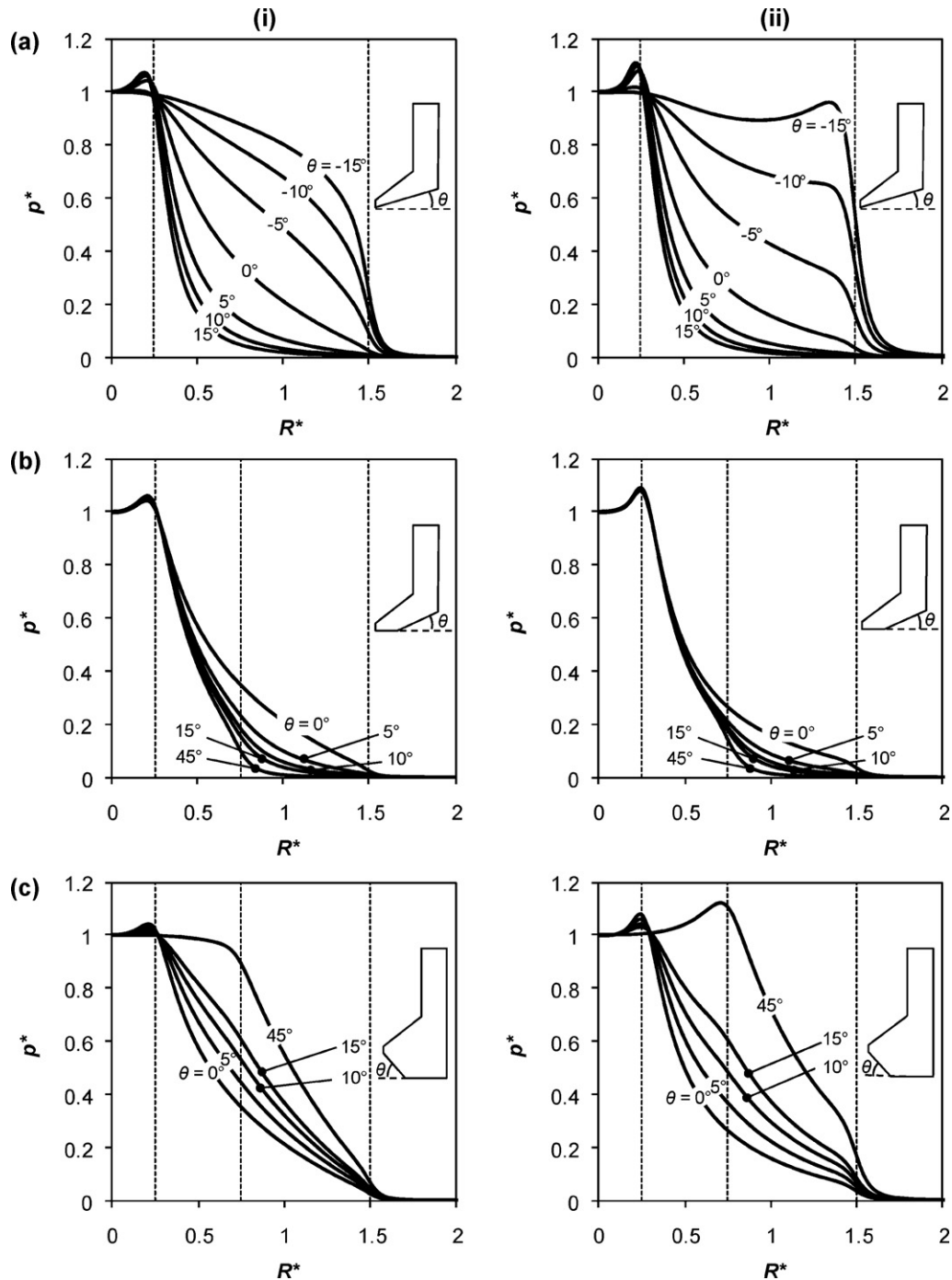


**Fig. 9 – Dimensionless pressure profiles for different values of  $\theta$  at  $h/d_t = 0.2$ . Nozzles: (a) N1; (b) N2, (c) N3: (i)  $Re = 50$ , (ii)  $Re = 500$ . Vertical dashed lines at  $R^* = 0.25$  and  $R^* = 1.5$  in (a) indicate the location of the outer and inner rim, respectively. In (b) and (c), dashed vertical lines at  $R^* = 0.75$  indicate the position of the transition on the nozzle surface.**

for nozzle N1 for positive values of  $\theta$  with a maximum in the range of  $R^* < 0.25$  and a gradual decrease until  $p^* = 0$  for  $R^* > 0.25$ . In these plots, the vertical dashed lines denote the location of the edges of the nozzle and the radius where the nozzle surface changes slope. The effect of  $\theta$  on the profiles is greater for lower  $Re$  and  $\theta < 10^\circ$ . These results were similar to those obtained for nozzle N1. For  $\theta = 45^\circ$ , the pressure profiles approached the data reported for a nozzle with  $\theta = 60^\circ$  in Chew et al. (2004a), indicating that an asymptotic profile was obtained. In all cases, the profiles showed a concave shape.

Profiles of dimensionless pressure for different values of  $\theta$  and  $Re$  for Nozzle N3 are shown in Fig. 9(c). The shape of the profiles are similar to those obtained for the other nozzles, with a maximum in  $p_0$  located near the nozzle throat and a

decreasing zone at higher  $R^*$  showing concavity and a slight linearity depending on the value of  $\theta$ . There are some important differences, however: (i) the pressure profiles showed different dependency of  $p^*$  on  $\theta$ , and (ii) the effect of  $\theta$  was less important in the range  $\theta < 10^\circ$ . This could be due to the nozzle throat being further from the gauged surface, producing a channeling effect on the flow. As seen for the previous nozzles, higher flow rates accentuated the profiles at the transition zones (vertical dashed lines), producing peaks and/or higher peaks.

#### 4.2.2. Shear stress

The profiles of dimensionless shear stress (defined as  $\tau^* = \tau/\tau_{max}$ , where  $\tau_{max}$  is the maximum value of the dimen-

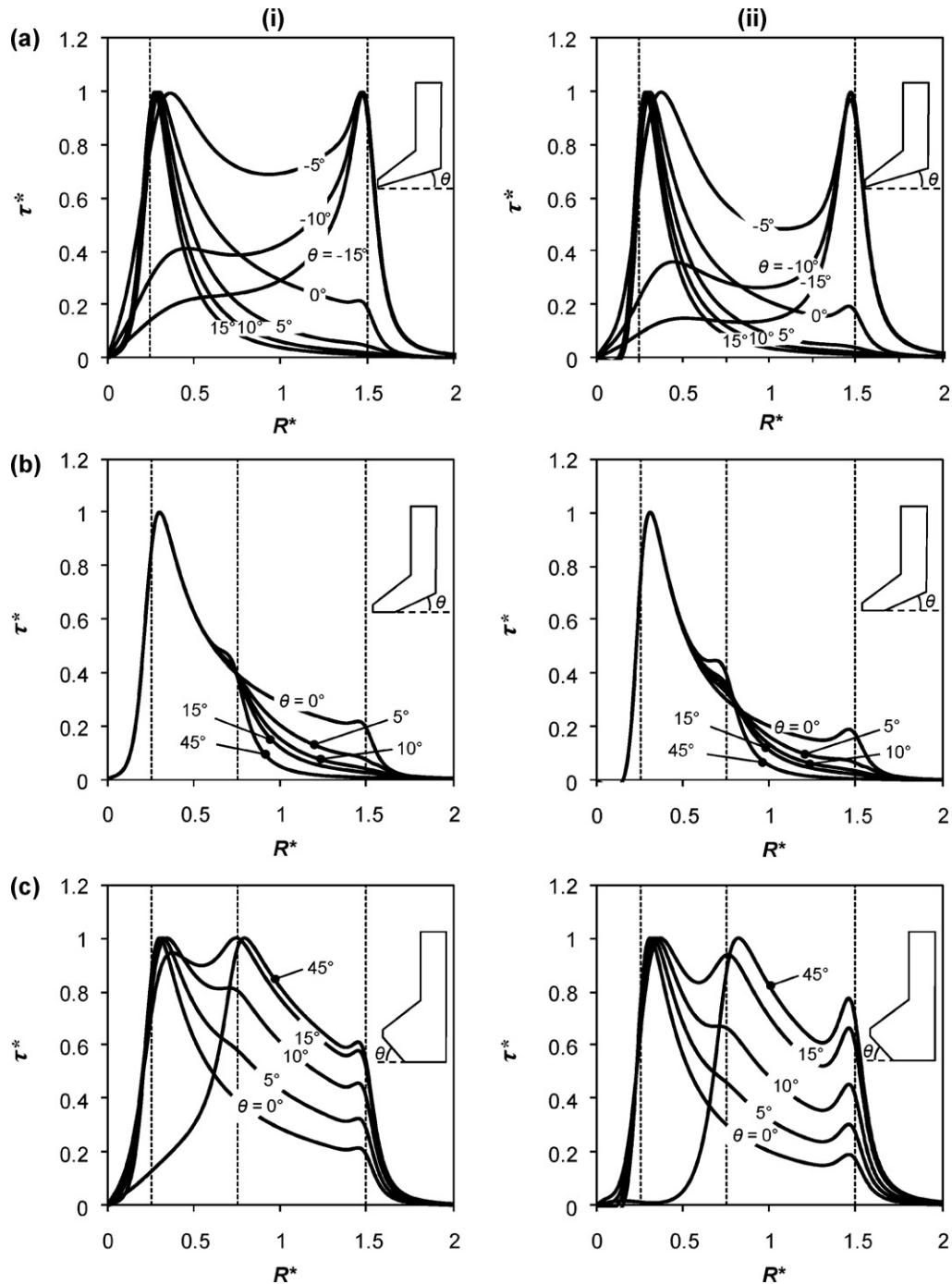


**Fig. 10 – Dimensionless shear stress as a function of dimensionless radial position for different values of  $\theta$  at  $h/d_t = 0.20$ . Nozzles: (a) N1; (b) N2, (c) N3: (i)  $Re = 50$ , (ii)  $Re = 500$ . Vertical dashed lines at  $R^* = 0.25$  and  $R^* = 1.5$  in (a) indicate the location of the outer and inner rim, respectively. In (b) and (c), dashed vertical lines at  $R^* = 0.75$  indicate the position of the transition on the nozzle surface.**

sional shear stress on the gauged surface under the nozzle) for Nozzle N1 are presented in Fig. 10(a). In general, the profiles exhibit a maximum value (in form of a peak) near the inner and the outer rims of the nozzle, their relative heights depending on  $\theta$ . The peaks in shear stress arise where high velocity gradients occur. The plots show that the shear stress distribution is strongly affected by nozzle shape, with the location of the maximum shear stress shifting from the inner to outer rim at  $\theta = 0^\circ$ . For  $\theta = 0^\circ$  and  $Re = 50$ , the results exhibit the form  $\tau \propto r^{-1}$  as predicted for radial flow in parallel disks (Middleman, 1998) and reported in previous simulations of FDG nozzles (Chew et al., 2004a,b). At higher  $Re$ , the peaks are more prominent (the shear stress falls away from the peak value more

strongly), which is expected since  $h$  is fixed and the velocity and velocity gradients will then scale with flow rate. An important finding from this work is that the region of highest shear stress shifts from the inner to the outer rim at negative  $\theta$ . A more even (albeit not linear) profile, linking two peaks, is observed for  $\theta = -5^\circ$  for both  $Re$  values. This ‘saddle’ shape suggests that nozzles of this geometry could be designed to exert an almost uniform shear stress on the surface being gauged, with obvious benefits for using the gauge to test the deformation of a deposit layer. This is explored further in Section 4.2.3.

Profiles of dimensionless shear stress as a function of dimensionless position for nozzle N2 are presented in



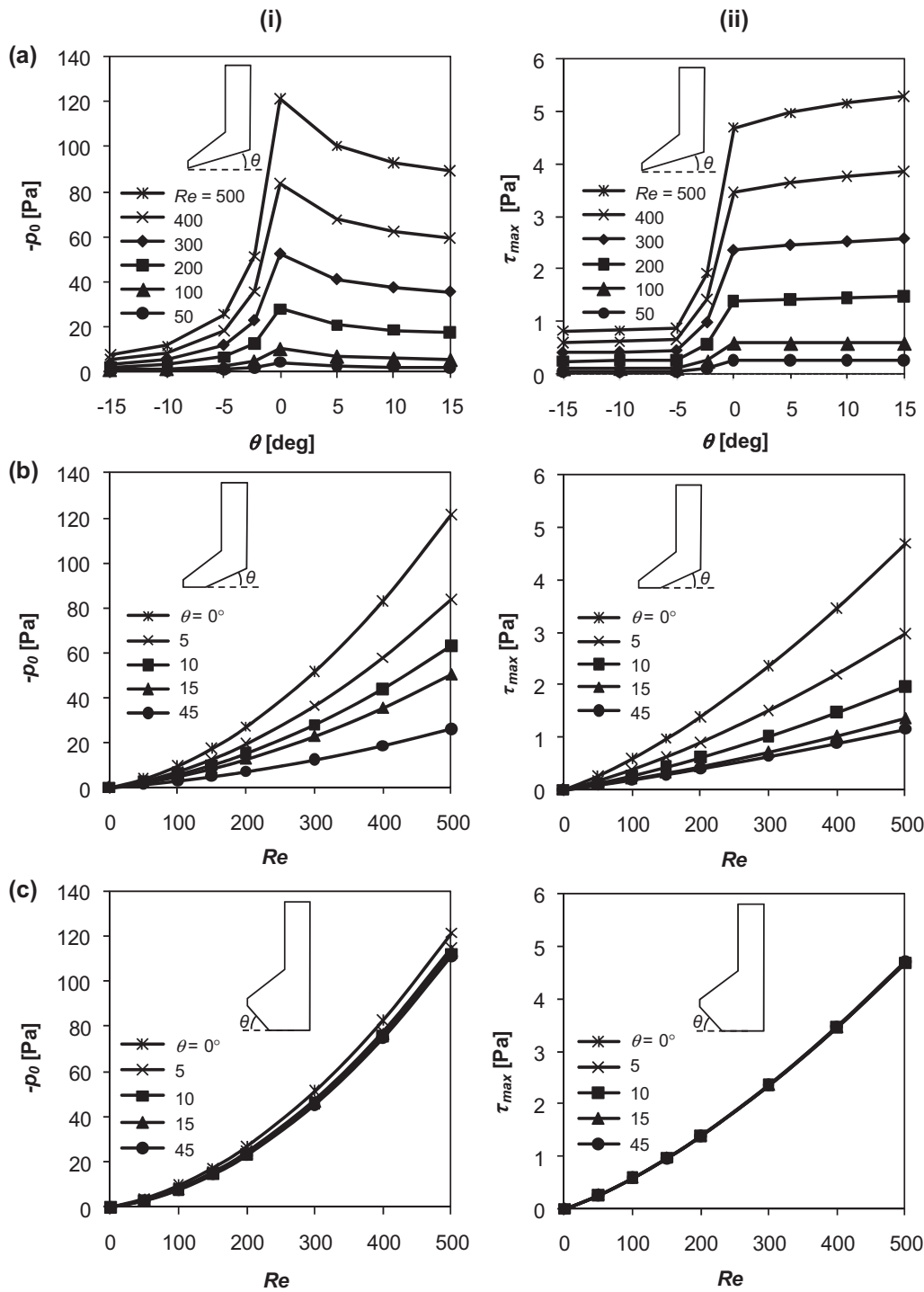


**Fig. 11 – Effect of Reynolds number and nozzle angle on pressure and shear stress profiles: Nozzles: (a) N1; (b) N2, (c) N3. Parameters: (i) pressure at the stagnation point, (ii) maximum shear stress on the gauged surface.**

Fig. 10(b). In this case, one main peak was found near the location of the inner radius and shoulders or small peaks were found near the zones of transition of the outer radius. Increasing  $\theta$  produced a gradual shift in the position of the small peaks, first changing them to a shoulder and then changing the position. These peaks are related to an increase in local velocity gradients resulting from the change in geometry, confirming the importance of the geometry on the flow behaviour. The effect of the slope on shear stress was relatively larger for lower  $Re$ , as observed with nozzle N1. Higher flow rates produced a steeper increase in shear stress which results in close profiles (data not shown). Again, as mentioned above for nozzle N1, the profiles were most sensitive to  $\theta$  in the range

$0 < \theta < 10^\circ$ . The shear stress profiles for N3 shown in Fig. 10(c) show a very strong effect of  $\theta$  for  $\theta < 15^\circ$ . As  $\theta$  increases, the pressure profiles present a more linear profile. This trend is accentuated at the lower  $Re$ . At  $\theta \sim 10^\circ$  an approximately linear, negatively sloping profile is obtained. For  $\theta \sim 15^\circ$ , the shear stress values in the inner zone of the rim present an almost uniform distribution. Finally, the peak observed at the inner radius moved to the transition point, at  $R^* = 0.75$ , for angles greater than  $15^\circ$ . These results show that the occurrence of the even profile in shear stress could also be sensitive to the dimensions of the nozzle.

There is a similar change in the profiles of dimensionless pressure and shear stress at  $\theta$  values between  $15^\circ$  and  $45^\circ$  for

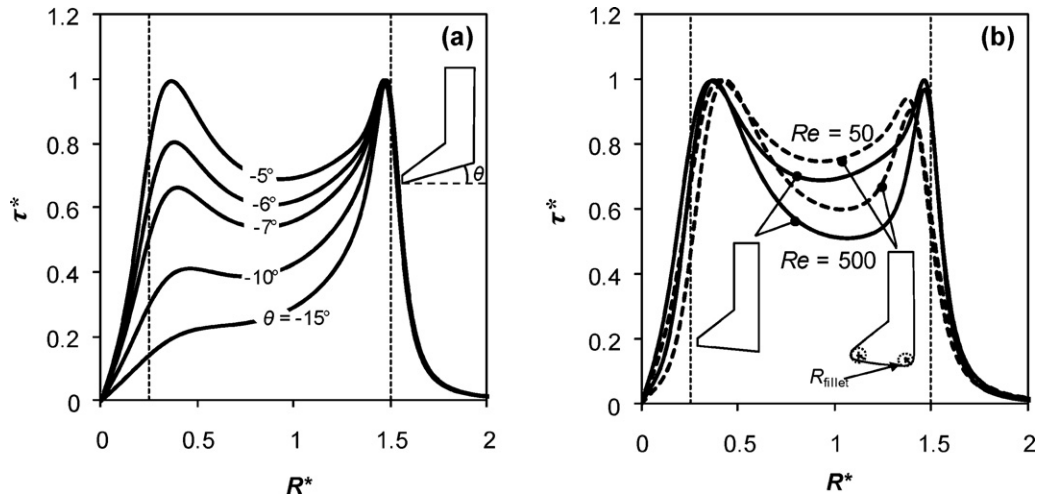


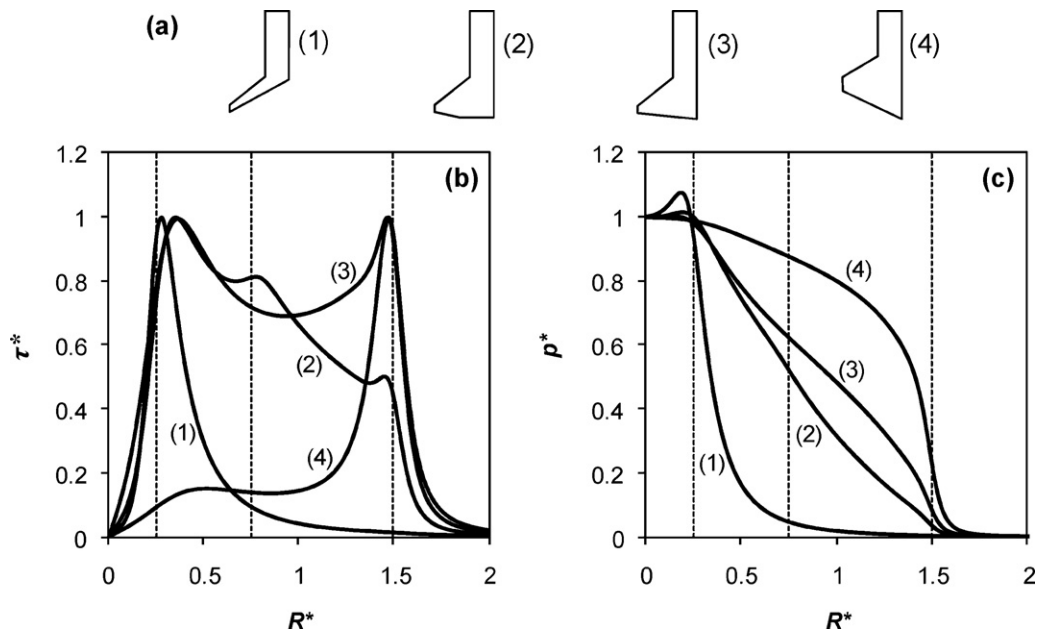
**Fig. 12 – Bimodal shear stress distributions with Nozzle N1: (a) effect of (negative) nozzle slop on bimodal shear stress distribution for  $Re = 50$ . (b) Comparison of the shear stress profiles for nozzle N1 with (dashed loci) and without (solid loci) rounded corners on the nozzle exterior ( $R_{\text{fillet}} = 1 \text{ mm}$ ).**

nozzle N2 (Figs. 9(b) and 10(b)), which is not observed with nozzle N3 (Figs. 9(c) and 10(c)). This is due to the fact that the maximum values of shear stress (taken as reference values for these dimensionless profiles) were affected differently when higher values of  $\theta$  were used. With nozzle N3, its position moves from the inner radius to  $R^* = 0.75$  as theta approaches  $45^\circ$ . Moving the throat of the nozzle away from the gauged surface results in a reduction in the shear stress value at the throat. In the case of pressure, the reference value is that at the stagnation point. Therefore, higher values of  $\theta$  (moving the throat of the nozzle away from the gauged surface) produced an asymptotic maximum value of pressure at the stagnation point and a plateau in the range  $0.25 < R^* < 0.75$ . This could be viewed as the nozzle throat diameter increasing from  $R^* = 0.25$  to  $R^* = 0.75$ .

The magnitude of the stresses generated depend on the flow rate as well as the nozzle geometry at a given  $h/d_t$ . Simulations were performed for type N1 nozzles with angle  $-15^\circ \leq \theta \leq 15^\circ$  and  $50 \leq Re \leq 500$ , and the results are summa-

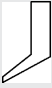




rized in terms of the pressure at the stagnation point,  $p_o$ , and the maximum shear stress on the gauged surface,  $\tau_{max}$ , in Fig. 11(a). A maximum in  $p_o$  was observed at  $\theta = 0^\circ$  for all values of  $Re$  studied, with non-symmetric dependency in  $\theta$ . For negative values, the pressure decreased with slope angle faster than for positive slopes. This is attributed to the fact that for negative angles, the nozzle throat is located further away from the surface in order to maintain  $h/d_t$  constant at the outer rim of the nozzle.  $p_o$  was found to be  $\propto Re^2$  for all values of  $\theta$ . On the other hand, the maximum shear stress values ( $\tau_{max}$ ) shift between two plateaus between  $-5^\circ < \theta < 0^\circ$  for all values of  $Re$  tested (Fig. 11(a)), with the values at positive  $\theta$  a factor of  $\sim 5 \times$  greater. These results suggest that nozzles with positive slopes be employed where large shear stresses are required and, conversely, negative slopes used where thickness measurements are to be made while imposing low shear stresses on the surface.

The maximum values of pressure and shear stress for N2 (Fig. 11(b)) exhibit a quadratic dependence on  $Re$  ( $\propto Re^2$ ). In this



**Fig. 13 – (a) Selected nozzle geometries and their (b) dimensionless shear stress and (c) pressure profiles for  $Re = 50$ . (1): Nozzles: (1) N1,  $\theta = 15^\circ$ ; (2) N3,  $\theta = 10^\circ$ ; (3) N1,  $\theta = -5^\circ$ ; and (4) N1,  $\theta = -15^\circ$ .**

**Table 1 – General types of dimensionless pressure and shear stress profiles for a Newtonian fluid on the gauged surface that could be found as a function of the external nozzle geometry.**

Type of geometry		Pressure profile	Shear stress profile
	Convergent with high values of $\theta$ (N1).	Sharp step with the maximum and a possible peak at the inner radius.	Peak with the maximum at the inner radius.
	Parallel to the gauged surface (N1).	Functionality of the type $\ln(1/r)$ for low $Re$ (Middleman, 1998).	Functionality of the type $1/r$ for low $Re$ (Middleman, 1998).
	First parallel to the gauged surface and then divergent with low values of $\theta$ (N3).	Approximately linear (for low $Re$ ) with the maximum at the inner radius.	Approximately linear (for low $Re$ ) with the maximum at the inner radius.
	Divergent with low ( $\theta \cong 5^\circ$ ) values of $\theta$ (N1).	Approximately linear (for low $Re$ ) with the maximum at the inner radius.	Approximately even with peaks at the inner and outer radius.
	Divergent with high values of $\theta$ (N1).	Concave for low $Re$ and with a possible peak for higher $Re$ .	Peak with the maximum at the outer radius and a shoulder at the inner radius.

case  $\theta$  has a relatively larger effect on the maximum values than with nozzle N1. This may be because the zone where these maximum values occur was located further from the gauged surface as  $\theta$  increased, resulting in lower maximum values.

Noticeably different trends in stagnation point pressure and maximum shear stress as a function of  $Re$  are evident for nozzle N3 in Fig. 11(c). The quadratic dependency on  $Re$  is again evident, but with little effect of  $\theta$  on  $p_o$  and  $\tau_{max}$  for all values of  $Re$  studied. In the case of  $p_o$ , only a 4% increase was observed as  $\theta$  changed from  $0^\circ$  to  $15^\circ$ , compared to a 33% change with nozzle N2. Moreover, no effect of  $\theta$  on  $\tau_{max}$  is seen with the N3 nozzle. This reduced sensitivity of  $p_o$  and  $\tau_{max}$  to  $\theta$  may be due to the fact that the location where these values occur remains at the same position in all simulations.

The maximum pressure and stress values discussed in the paragraphs above are local, peak values: for certain applications a more even distribution of shear stress is desirable. Fig. 10(a) and (b) showed a bimodal distribution in  $\tau^*$  for  $\theta = -5^\circ$ , and the sensitivity of this bimodality to  $\theta$  is presented in Fig. 12(a). The bimodality is lost at  $\theta < -10^\circ$ , indicating that some precision would be required in fabricating the nozzle. Some machining features can, however, be allowed without losing the desired effect: Fig. 12(b) shows shear stress profiles for N1 nozzles with  $\theta = -5^\circ$  with and without filleted corners. The bimodality is preserved, with the position of the peaks being shifted away from the nozzle rims and, furthermore, the shear stress being more evenly distributed between the peaks.

#### 4.2.3. Nozzle comparison

Certain nozzle geometries were chosen for further study based on the above analysis of shear stress and pressure profiles. The nozzles selected are shown in Fig. 13(a) along with their shear stress and pressure profiles (Fig. 13(b) and (c)), respectively. These nozzles produced saddle-like, linear or spiked profiles of shear stress on the gauged surface, which are very different from the shear stress profiles reported for the 'standard'

conical configurations by Chew et al. (2004a,b). In terms of the pressure, nozzles (2) and (3) exhibit an almost linear decrease with radius, which is consistent with the more even shear stress profiles.

Table 1 summarizes some general relationships between the geometry and the pressure and shear stress profiles exerted on the gauged surface for a Newtonian fluid deduced from these investigations. These can be used as guidelines for selecting FDG nozzles with particular combinations of parameter magnitude or parameter distribution.

## 5. Conclusions

The effect of the external nozzle geometry used in fluid dynamic gauging on the shear stress and pressure exerted on the gauged surface has been investigated. Three geometries were compared *in silico* using computational fluid dynamics simulations, investigating the effect of slope and  $Re$ . Mesh independence testing indicated that the numerical results were reliable and comparison between experimental pressure values obtained one nozzle geometry showed good agreement with the numerical predictions.

In general, nozzle geometry had more influence on the shape of the shear stress and pressure distributions than  $Re$ . Interesting shear stress and pressure profiles, including ones where these parameters were approximately constant or changed linearly with radius, were observed for certain nozzle geometries and  $Re$  values.

This work shows that it is possible to manipulate the external shape of the nozzle to obtain particular shear stress and pressure profiles on the gauged surface. The desired profile will depend on the particular application of the FDG technique, for instance surface rheology testing or precision thickness measurement. Future studies will investigate nozzle shapes to deliver particular stress distributions and methods to determine the nozzle shape required for a given application more directly.

## Acknowledgments

JMP wishes to acknowledge Drs Susana Zorrilla and Amelia Rubiolo for their invaluable support during his postdoctoral visit to the group at Cambridge, and the financial support from the Consejo Nacional de Investigaciones Científicas y Técnicas (CONICET) and Universidad Nacional del Litoral of Argentina. A Royal Academy of Engineering/EPSC Research Fellowship for YMJC is also gratefully acknowledged.

## References

- Chew, Y.M.J., Cardoso, S.S.S., Paterson, W.R., Wilson, D.I., 2004a. CFD studies of dynamic gauging. *Chemical Engineering Science* 59 (16), 3381–3398.
- Chew, Y.M.J., Paterson, W.R., Wilson, D.I., 2004b. Fluid dynamic gauging for measuring the strength of soft deposits. *Journal of Food Engineering* 65 (2), 175–187.
- COMSOL, 2008. COMSOL Multiphysics Reference Guide. COMSOL AB, Hatfield, UK.
- Epstein, N., 1983. Thinking about heat transfer fouling: a  $5 \times 5$  matrix. *Heat Transfer Engineering* 4 (1), 43–56.
- Gordon, P.W., Brooker, A.D.M., Chew, Y.M.J., Wilson, D.I., York, D.W., 2010. Studies into the swelling of gelatine films using a scanning fluid dynamic gauge. *Food and Bioprocess Processing* 88 (4), 357–364.
- Hooper, R.J., Liu, W., Fryer, P.J., Paterson, W.R., Wilson, D.I., Zhang, Z., 2006. Comparative studies of fluid dynamic gauging and a micromanipulation probe for strength measurements. *Food and Bioprocess Processing* 84 (4C), 353–358.
- Middleman, S., 1998. *An Introduction to Fluid Dynamics. Principles of Analysis and Design*. John Wiley & Sons, New York.
- Sahoo, P.K., Chew, Y.M.J., Mercadé-Prieto, R., Wilson, D.I., Dai, X.W., 2008. Fluid dynamic gauging studies of swelling behaviour of whey protein gels in NaOH/NaCl solutions. *International Journal of Food Science and Technology* 43 (10), 1901–1907.
- Saikhwan, P., Chew, Y.M.J., Paterson, W.R., Wilson, D.I., 2007. Swelling and its suppression in the cleaning of polymer fouling layers. *Industrial and Engineering Chemistry Research* 46 (14), 4846–4855.
- Tuladhar, T.R., Paterson, W.R., Macleod, N., Wilson, D.I., 2000. Development of a novel non-contact proximity gauge for thickness measurement of soft deposits and its application in fouling studies. *Canadian Journal of Chemical Engineering* 78 (5), 935–947.